Available online at www.sciencedirect.com
ScienceDirect
International Journal of Heat and Mass Transfer 50 (2007) 4063–4078
International Journal of HEAT and MASS TRANSFER
www.elsevier.com/locate/ijhmt

High rotation number heat transfer of a 45° rib-roughened rectangular duct with two channel orientations

T.M. Liou [a,*], S.W. Chang [b], J.H. Hung [a], S.F. Chiou [b]

[a] Department of Power Mechanical Engineering, National Tsing Hua University, 30013 Hsinchu, Taiwan, ROC
[b] Department of Marine Engineering, National Kaohsiung Marine University, No. 142, Hai-Chuan Road, Nan-Tzu District, 811 Kaohsiung, Taiwan, ROC

Received 2 August 2006; received in revised form 13 November 2006

Abstract

An experimental study of heat transfer in a radially rotating rectangular channel of aspect ratio 1/2 with two opposite walls roughened by 45° staggered ribs is performed. Heat transfer distributions along centerlines of two rib-roughened surfaces are measured for the radially outward airflow at test conditions of Reynolds number (*Re*), rotation number (*Ro*) and density ratio ($\Delta\rho/\rho$) in the ranges of 5000–15,000, 0–2 and 0.07–0.28. The rotating test rig permits the generation of heat transfer data with *Ro* considerably higher than previous data ranges. A selection of experimental data illustrates the individual and interactive influences of *Re*, *Ro* and buoyancy number (*Bu*) on local heat transfer with two channel orientations of 0° and 45°. With *Ro* varying from 0.1 to 2, heat transfer ratios between rotating and static channels on the stable and unstable rib-roughened surfaces with 0° (45°) of channel orientation are in the ranges of 0.5–1.42 (0.5–1.49) and 1.08–2.73 (1.06–2.21) respectively. A set of heat transfer correlations for the test geometry with channel orientations of 0° is derived to evaluate the local Nusselt number (*Nu*) in the periodically developed region with *Re*, *Ro* and *Bu* as the controlling flow parameters.

Keywords: 45° angled and staggered ribs; Channel orientation; High rotation number; Density ratio; Turbine rotor blade cooling

1. Introduction

Modern gas turbine rotor blades are internally cooled by circulating pressurized airflow through multipass rib-roughened passages with 180° turns to connect the consecutive passages. The rib-roughened coolant passages have a variety of rib arrangements and cross-sectional shapes, which vary from the blade-nose to the midchord. The tail-end passage, which has bleeding holes to discharge air for regional cooling or fitted with pin-fin array for heat transfer augmentation is nearly triangular with a very low aspect ratio cross-section. The channel orientation relative to the rotating direction also changes from the blade-nose to blade-tail. Experimental heat transfer data as the function of flow parameters, the passage geometries, the channel orientation and the rib configurations *at engine representative conditions* is essential in order to evaluate material temperatures and life of turbine rotor blades.

Coolant passages in a gas turbine rotor blade rotate about an axis orthogonal to the main flow direction. Rotation manifesting effects on the mean flow pattern as well as the turbulence structure provide consequential influences in the cooling performance. Rotation induced Coriolis force establishes cross-stream pressure gradients which drive the relatively cool fluids from the central core region towards the unstable side of channel, leading to the generation of Coriolis secondary flows perpendicular to the main flow direction. Turbulence is enhanced on the unstable side but suppressed on the stable side of an orthogonally rotating channel. Beyond a critical rotation number (*Ro*), Coriolis forces generate *Ro* dependent spanwise roll-cells that make a significant contribution to total turbulence quantities [1]. Heat transfer rates on the unstable surface of a rotating passage are consequently improved in relation to

* Corresponding author. Tel.: +886 3 572 9716.
E-mail address: tmliou@pme.nthu.edu.tw (T.M. Liou).

0017-9310/$ - see front matter © 2007 Elsevier Ltd. All rights reserved.
doi:10.1016/j.ijheatmasstransfer.2007.01.060

Nomenclature

A, n	coefficient
Bu	Buoyancy number $= Ro^2\beta(T_w - T_b)(R/d)$
C_p	specific heat of fluid (J kg^{-1} K^{-1})
d	hydraulic diameter of test duct (m)
e	rib height (m)
H	channel height (m)
k	thermal conductivity of fluid (W m^{-1} K^{-1})
l	rib land (m)
Nu	Nusselt number $= qd/[k(T_w - T_b)]$
Nu_0	zero rotation Nusselt number
Nu_∞	Nusselt number value for stationary developed turbulent duct flow
P	rib pitch (m)
Pr	Prandtl number $= \mu C_p/k$
q	convective heat flux (W m^{-2})
R	mid-span eccentricity of test channel (m)
Re	Reynolds number $= \rho W_m d/\mu$
Ro	Rotation number $= \Omega d/W_m$
T_b	fluid bulk temperature (K)
T_w	wall temperature of test duct (K)
W	channel width (m)
W_m	mean through flow velocity (m s^{-1})
x	axial location (m)
X	dimensionless axial location $= x/d$

Greek symbols

α	rib angle of attack (°)
β	thermal expansion coefficient of fluid (K^{-1})
ρ	fluid density (kg m^{-3})
μ	fluid dynamic viscosity (Pa s)
λ	angle of channel orientation (°)
Ω	rotating speed of test duct (rad s^{-1})
Ψ, ϕ_1, ϕ_2	unknown functions

Subscripts

L	refers to centerline of rotating leading-wall
T	refers to centerline of rotating trailing-wall
0	refers to non-rotating situation

that on the stable surface. Centrifugal forces acting on the coolant in a rotating passage interact with the temperature dependent density field to motivate a buoyancy-type alteration to the flow field. The angular acceleration of a typical rotor blade is up to 50,000g that amplifies the rotating buoyancy effects. However, the operating temperatures of a gas turbine rotor blade, the complex internal cooling configurations as well as the extremely high rotational speed have combined to oppose the progress in acquiring the laboratory-scale heat transfer data with a full coverage of engine conditions. Many studies on rotor blade cooling have been confined to low Ro with the simplified channel geometries.

A number of experimental studies have been performed to study the flow and heat transfer in rotating passages with turbulence promoters [2–17]. The presence of surface ribs in a rotating channel induces the rib-triggered flow separation and reattachment that leads to a general rise in turbulence and heat transfer levels. Flow mechanism in a rotating channel is complicated by the interaction of Coriolis forces with rib-wise secondary flows as well as longitudinal separation flows adjacent to ribs. With a set of pre-defined thermal boundary conditions, the geometrical parameters relevant to the cooling performance of a rotating passage include the configuration of surface roughness [2–17], the channel orientation and cross-sectional shape [2,5,6,8], the pin-fin configuration [17] and the multi-pass passages connected by 180° turns [2,6,9–17]. Parametric studies of heat transfer in rotating passages customarily adopt the flow parameters of Reynolds (Re) and rotation numbers to characterize the relative strengths of forced convection and Coriolis secondary flows in their own rights. The buoyancy effect is often indexed by density ratio, $\Delta\rho/\rho$, where the density difference ($\Delta\rho$) is defined as the coolant's density variation from the reference density, ρ, at a selected temperature datum. In the attempt to quantify the relative strength of *rotating* buoyancy force, the combination of density ratio ($\Delta\rho/\rho$), Ro^2 and rotating radius (R/d) in the form of $\Delta\rho/\rho Ro^2$ (R/d) is used to level the rotating buoyancy. A selection of experimental works investigating rotational influences on flow and heat transfer at various test conditions are summarized in Table 1 that depicts the relevant flow and geometrical parameters examined by different research groups [2–17].

Reynolds numbers attempted by the previous studies collected in Table 1 are in the range of 5000–75,000 with the rotation numbers ranging from 0 to 1. Reductions of Reynolds number ($Ro = \Omega d^2\rho/(Re\mu)$) to elevate the rotational number have been a long term approach for laboratory-scale experiments. This approach comprises the opportunity to stimulate the turbulence structures for high Re flows which consequently undermines the reality of rotational influences on turbulence for laboratory-scale experiments. Typical gas turbine engine speeds are in the range of 3000–20,000 rev/min with maximum Re of 100,000 for the coolant channel flow. The maximum Ro experienced by the coolant passage in a gas turbine rotor blade reaches 2 [18]. There is a strategic need to extend the experimental data to emulate more closely realistic engine conditions by extending Re and Ro simultaneously. To acquire the laboratory-scale simulations with Re, Ro and $\Delta\rho/\rho$ simultaneously matching the realistic engine conditions, the recent developing trend for experimental studies is directing toward the high pressure tests with large hydraulic diameter of test channel. A preliminarily trial test using this experimental approach for rotating channel flow

Table 1
Experimental heat transfer in rib-roughened rotating channel

Group	Surface condition	*Ro*	*Re*	Max. $Re \times Ro$	$\Delta\rho/\rho$
Chang et al.[a]	45° staggered rib [2]	0–1	5000–15,000	15,000	0.076–0.294
Han et al.[b]	Dimples [3]	0–0.3	5000–40,000	1500	0.122
	45° parallel rib [4]	0–0.3	5000–40,000	1500	0.122
	45° V-Shaped rib [5]	0–0.21	5000–40,000	1050	0.115
	Half-V rib [6]	0.03–0.3	5000–25,000	1500	0.13
Morris et al.[b]	0° parallel rib [7]	0–0.42	25,000	4200	0–0.223
	45° staggered rib [8]	0–1.0	20,000–45,000	20,000	0–0.00448[c]
	45° staggered rib [8]	0–0.8	20,000–45,000	16,000	0–0.00403[c]
Liou et al.[b]	0° parallel rib [9]	0–0.2	10,000	2000	0.05–0.058
	0° detached rib [10]	0–0.2	10,000	2000	0.055–0.221
Hsieh et al.[b]	0° parallel rib [11]	0–0.09	5000–10,000	450	Not examined
Yang et al.[b]	45°, 60°, 0° parallel rib [12]	0–0.139	10,240–31,300	1423	Not examined
Hwang et al.[b]	Staggered half V rib [13]	0–0.21	20,000–40,000	4200	0.229
Johnson et al.[b]	0° staggered rib [14]	0–0.48	12,500–50,000	12,000	0.07–0.22
	45° staggered rib [15]	0–0.36	12,500–75,000	9000	0.07–0.22
Taslim et al.[b]	60° rib [16]	0–1.78	5000–23,000	8900	Not examined
Bergles et al.[b]	Pin-fin duct [17]	0–0.21	6900–17,200	1450	0.045–0.095

[a] The highest rotation number is achieved for each Reynolds number tested.
[b] The highest rotation number is achieved for the lowest Reynolds number tested.
[c] Buoyancy level is indexed by $\beta\tau d$ where τ represents streamwise fluid bulk temperature gradient.

has generated a set of heat transfer data in the range of $Re \times Ro \leqslant 10{,}000$ and $Ro = 1$ [2]. The present study follows the similar experimental strategy to generate the heat transfer results in a rectangular duct fitted with staggered 45° ribs that are closely approaching the engine conditions.

An experimental study aimed at determining the individual and interactive influences of inertial and Coriolis forces with and without buoyancy interaction on heat transfer is performed using a rib-roughened rectangular channel with an aspect ratio of 1/2. The engineering methodology in the attempt to generate heat transfer correlation is presented. Impacts of channel orientation on rotational effects are examined by comparing two sets of rotational heat transfer data generated with channel orientations of 0° and 45°. Heat transfer data generated by present study reveals the heat transfer physics in the rotating rib-roughened channel with high rotation numbers up to 2. The empirical heat transfer correlation that shows numerical consistencies between the correlative results and actual measurements is applicable to the design of coolant channel in a gas turbine rotor blade.

2. Experimental details

2.1. Apparatus

The mechanical layouts of rotating rig, the instrumentations for the measurements of flow, heating-power and temperature and the method of data acquisition adopted by present study have been previously reported [2]. This rotating rig was designed, constructed and commissioned to perform high pressure tests in order to elevate *Ro* values. Pressure levels for present heat transfer tests are controlled in the range of 1.66–3.223 bars to allow for the full coverage of test conditions. The rotating rig was configured to carry a 246 mm long heat transfer test section with a mid-span eccentricity (R) of 373 mm at speeds up to a nominal value of 850 rev/min. Test coolant, air, is pressurized by IWATA SC 175C screw-type compressor unit. The coolant flow is dehumidified and cooled to ambient temperature through a refrigeration unit. The dehumidified airflow is channeled through a set of pressure regulator and filter, a pressure transducer, a Tokyo Kesio mass flow meter and a needle valve that controls the mass flow rate of coolant. Adjustments of coolant's mass flow rate are frequently made to compensate the variations of fluid properties in order to maintain the variations of *Re* and *Ro* at the flow entrance of test section within $\pm 1\%$ of the targeting values. The metered airflow is then entered the rotating test rig and heat transfer test channel.

Fig. 1 shows the heat transfer test module with airflow in the radially outward direction. The test section is rectangular in cross-section with a channel height to width ratio of 1/2. This test channel is made up of leading (1) and trailing (2) heated walls, together with two Teflon side walls (3). The constructional walls are physically held together by means of a series of axial bolts to form the rectangular channel with hydraulic diameter (d) of 30 mm. Heat transfer measurements and heat fluxes are provided over two opposite rib-roughened leading (4) and trailing (5) foils. Each of these two rib-roughened heating foils is produced by forging a continuous 45 mm wide, 0.1 mm thick stainless-steel foil that provides 246 mm long electrically heated surface. Electrical heating power is connected in series to heat two ribbed foils with the basically uniform heat flux thermal boundary condition. Surface ribs of attack angle 45° are arranged in the staggered manner on two opposite walls. The present heating surface also issues uniform heat flux from the top and side walls of each skewed rib. This type of heating condition is different form those using the

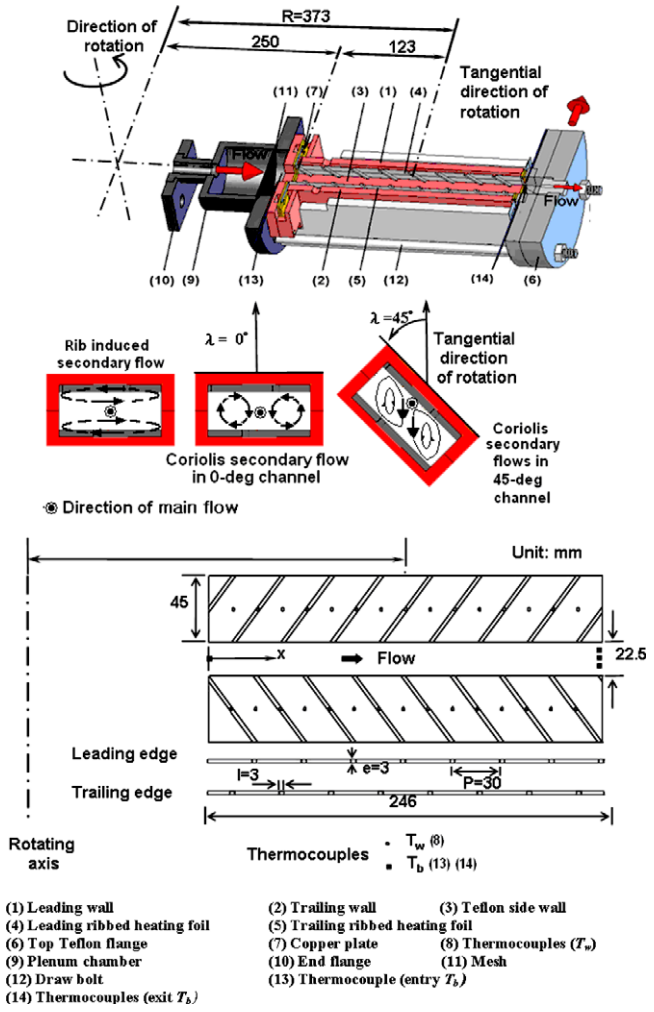

Fig. 1. Heat transfer test module with conceptual secondary flow petterns looking toward the downstream direction.

heating foil underneath a rib-roughened plate. Differences in the thermal boundary conditions between present and previous studies [3–15] can result in different rotating-buoyancy impacts on heat transfer. The surface areas of all skewed ribs are taken into account for the evaluation of realistic heat flux. Electrical DC currents through the stainless-steel heating foils (4) and (5) are converted from a Variac transformer with the power consumption metered by a Wattmeter. Adjustments of heating power modify the relative strengths of buoyancy level at each tested *Re* and *Ro* combination that enable the investigation of buoyancy in isolation. These two rib-roughened heating foils are clamped between the top Teflon flange (6) and two bottom copper plates (7) to secure their positions in the test channel. Under the top Teflon flange (6), a 3 mm thick copper plate is sandwiched between the top flange (6) and two heating foils to complete the electrical circuit. A replaceable orifice thread is fitted at the center of top Teflon flange (6). Adjustment of pressure level in the test channel is achieved by replacing the orifice thread with different throat area. Adequate combinations of test pressure and rotating speed allow both *Re* and *Ro* to be controlled at the predefined values.

Along the centerline of each rib-roughened surface, 15 K-type thermocouples (8) with equal intervals are sparkle-welded on the back of the stainless-steel heating foil to measure the centerline wall temperature distributions on the leading and trailing surfaces. The diameter of thermocouple wire is 0.1 mm so that the thermal leakage from these thermocouple wires is negligible. At the rib location, the thermocouple is welded at the center of rib land where spans 1.5 mm from the edge of the top face of the rib. Thermocouple measurements are limited by the available channels of instrumentation slip rings. Heat transfer results revealed by this study can not be treated as the surface averaged tendency so that the influences of channel orientation on heat transfer over two rotating rib floors are examined at the locations along the centerlines of leading and trailing-walls. The coordinate system and the locations of these thermocouples that correspond to the rib and mid-rib locations are indicated in Fig. 1. Ceramic cement is inserted at each thermocouple junction to secure its position on the heating foil. Thermocouple wires and heater cables are taken out of the test section through the grooves machined on the Teflon leading and trailing-walls to connect with the instrumentation and power slip rings. These grooves are filled with the sealant of low heat resistant that can sustain high temperatures in order to inhibit air leakage. Although peripheral heat transfer variations over each rib-roughened surface as a reflection of the interactive mechanism between Coriolis and rib-induced secondary flows are expected, the limited channels of instrumentation slip-rings prohibit the additional installations of rib-wise thermocouples. The peripheral heat transfer variation over each rib-roughened surface is not investigated by present study.

Geometric features of the single-pass rib-roughened rectangular channel are characterized by five dimensionless parameters of

Channel height, H(22.5 mm)/channel width, W(45 mm) = 1/2
Rib angle of attack, $\alpha = 45°$
Rib height, e(3 mm)/channel hydraulic diameter, d(30 mm) = 0.1
Rib pitch, P(30 mm)/rib height, e(3 mm) = 10
Rib land, l(3 mm)/rib height, e(3 mm) = 1

A cylindrical plenum chamber (9) consolidated with the end flange (10) is mounted on the rotating test platform. This plenum chamber in conjunction with the heat transfer test assembly is preset at an angular position on the rotating platform so that the test cannel can spin at a predefined channel orientation (λ) as indicated in Fig. 1. Two sets of rotating tests with channel orientations of $\lambda = 0°$ and 45° are performed by present investigation. Several layers of fine mesh (11) are installed at the exit of plenum chamber. The complete set of test assembly is tightened between the

end and top flanges (6) and (10) by four draw-bolts (12). Air leakage from each pair of jointed faces is prevented by means of a series of 'O' ring seals.

Entry air temperatures are measured by a thermocouple (13) penetrating into the plenum chamber. *Re* and *Ro* at the flow entrance of test section are referred to as the targeting values for experimental tests with fluid properties evaluated from the measured air inlet temperature. Fluids properties used to define local *Re*, *Ro*, *Bu* and *Nu* are based on the local fluid bulk temperatures. Three thermocouples (14) at three different spanwise locations on the exit plane of test section as indicated in Fig. 1 measure the airflow exit temperatures. The fluid bulk temperature at exit plane of test section is approximated as the average of three temperature measurements detected from these thermocouples (14). The enthalpy balance method is employed to determine the fluid bulk temperatures at the axial locations where T_w are measured. The calculated fluid bulk temperature at the exit plane of test section is compared with the actual measurement to check the accuracy of energy conservation as well as the flow leakage. Experimental raw data is collectable only if the difference between calculated and measured fluid bulk temperatures at the exit plane of test section is less than ±10%. Thermal insulation material is packed on the outer surface of test module to minimize the external heat loss.

Examination of the dimensionless momentum conservation equations expressed relative to a rotating reference frame as well as the energy equation suggests that the following non-dimensional groups can be used to characterize the local heat transfer for a set of predefined geometrical parameters of test channel and thermal boundary condition.

$$Nu = qd/k(T_w - T_b) \quad \text{Nusselt number} \tag{1}$$

$$Re = \rho W_m d/\mu \quad \text{Reynolds number} \tag{2}$$

$$Ro = \Omega d/W_m \quad \text{Rotation number} \tag{3}$$

$$Bu = Ro^2\beta(T_w - T_b)(R/d) \quad \text{Buoyancy number} \tag{4}$$

$$Pr = \mu C_p/k \quad \text{Prandtl number} \tag{5}$$

$$X = x/d \quad \text{Axial location from flow entrance of test duct} \tag{6}$$

All symbols in Eqs. (1)–(6) are as defined in the Nomenclature section. In order to determine the local variation of the convective heat flux to the fluid (q in Eq. (1)), a careful energy balance involving the generation of heat flux in the electric foil and external loss to atmosphere is employed as described by Chang et al. [2]. The extent and characteristics of external heat loss are acquired by means of a series of static and rotating heat loss calibration tests that are individually performed prior to the heat convection tests. For this class of experimentation, the maximum heat loss is about 10.2% of the total heat flux supplied, taking place at the highest rotation speed, *Re* and T_w tested.

2.2. Program

The well known non-dimensional heat transfer relationships for forced convection in ducts that include the rotation induced groups are summarized by an equation, having the structure

$$Nu = \Psi(Re, Ro, Bu, Pr, X) \tag{7}$$

Variations of the governing dimensionless group, such as *Re*, *Ro*, *Pr* or *Bu*, for a set of pre-defined geometrical and thermal boundary conditions cause corresponding heat-transfer variations in a rotating channel. The strategic aim of present study is to disclose the functional relationship of Eq. (7). With T_b varying from 33.8 to 88.7 °C, variations in *Pr* of coolant are limited within ±0.82% that is considered as negligible. The *Pr* impact on heat transfer is disregarded from Eq. (7).

Table 2 summarizes the values of non-dimensional groups tested. The maximum *Re* and *Ro* in Table 2 are not simultaneously attainable. The test range of $0 \leqslant Ro \leqslant 2$, which accordingly increases the *Bu* range has considerably extended the data range available in the open literature.

Experiments with zero rotational speed are initially performed to validate the reliability of test facility by comparing these results with relevant studies. These zero-speed tests generate a reference data-base to which the rotational results are compared. A series of rotating experiments that control both *Re* and *Ro* at the predefined values by adjusting rotational speeds and pressure levels in the test section is followed. To examine the effects of rotating buoyancy in isolation, tests with five ascending heater powers to raise the highest wall temperatures to 75, 100, 125, 140 and 150 °C are performed for each set of *Re*–*Ro* combination. All the measurements are taken when the steady-state assumption is satisfied by the experimental condition. Steady state conditions are approximated when T_w variations for several successive scans are less than ±0.3 °C. Time intervals between two successive scans are about 60 s. Having satisfied the steady-state condition, all the relevant measurements are acquired and processed into the dimensionless groups defined in Eq. (7) with the fluid properties calculated from local fluid bulk temperatures. Individual and interactive impacts of *Re*, *Ro* and *Bu* on heat transfer are subsequently analyzed with a set of heat

Table 2
Tested values of experimental non-dimensional parameters

Non-dimensional parameter	Tested values
Reynolds number [*Re*]	5000, 7500, 10,000, 12,500, 15,000
Rotation number [*Ro*]	0, 0.1, 0.3, 0.5, 0.7, 1, 1.3, 1.5, 1.7, 2
Buoyancy number $[Bu = \beta(T_w - T_b)Ro^2(R/d)]$	0.005–8.879
Density ratio $[\Delta\rho/\rho = \beta(T_w - T_b)]$	0.07–0.28
Maximum $Re \times Ro = 15{,}000$ ($Re = 15{,}000$, $Ro = 1$)	

transfer correlations generated to calculate the local Nusselt numbers on rib and mid-rib locations in the periodically developed region. Nevertheless, the acquisition of experimental heat transfer data requires a finite wall-to-fluid temperature difference so that the interactive buoyancy impact on *Nu* data is inevitable. Heat transfer results affected by individual *Re* or *Ro* impacts without buoyancy interaction are obtained by extrapolating the rotational heat transfer data into the limiting condition of $Bu = 0$ with *Re* and *Ro* remain at finite values. Inclusions of the extrapolating heat transfer data at the so-called zero-buoyancy condition complete the entire set of heat transfer results.

Experimental uncertainties in calculating the dimensionless groups of Eq. (7) are mainly attributed from the temperature measurements as the fluid properties are calculated using the equations with T_b as the determining variable. Test results with the higher heating power and Reynolds number indicate the reduced experimental uncertainties. The wall-to-fluid temperature differences for the present data set are in the range of 21–98 °C. Following the method of estimating experimental uncertainties documented in ASME J. Heat Transfer [19], the maximum uncertainties for *Nu*, *Re*, *Ro* and *Bu* are about 9.6%, 5.2%, 4.8% and 8.9% respectively.

3. Results and discussion

3.1. Heat transfer results with zero rotation

Experimental results with zero rotational speed demonstrate that the staggered arrangement of surface ribs generates wall temperature differences between two opposite measurement spots on the leading and trailing-walls due to the different flow structures developed at the rib and mid-rib locations. Axial distributions of wall temperatures follow a zigzag pattern with the lower temperatures detected at the rib locations relative to the downstream mid-rib spots. Cooling air bulk temperatures increase linearly in the direction of flow as the thermal boundary condition corresponds closely to the uniform heat flux. By way of normalizing local Nusselt number at zero rotational speed (Nu_0) with Dittus–Boelter Nusselt number (Nu_∞) [20], heat transfer enhancements from the smooth-walled tube level due to the surface ribs are realized. Fig. 2 shows the typical form of the axial distributions of Nu_0/Nu_∞ along the centerlines of leading and trailing surfaces. The processed Nusselt number ratios (Nu_0/Nu_∞) along the test channel follow the zigzag pattern with the higher cooling rates developed at the rib tops. The separated flow triggered at the top corner of the front face for each rib along with the elevated turbulence level in a static rib-roughened channel are reported to produce the higher regional heat transfer rates on the rib tops [21]. Heat transfer ratios (Nu_0/Nu_∞) measured individually on the leading or trailing edge are similar for five heater power settings used, which suggests the negligible buoyancy impact on heat transfer

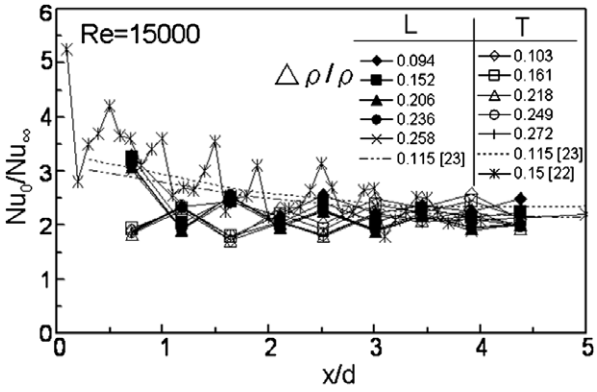

Fig. 2. Local Nusselt number distributions along leading and trailing edges for various $\Delta\rho/\rho$ at $Re = 15{,}000$ and $Ro = 0$.

in static channel. The similar Nu_0/Nu_∞ profiles along both instrumented edges of test channel are constantly detected for all the tested Reynolds numbers but with different heater power settings. This result confirms that T_b induced property variations are being adequately accounted by the normal process of non-dimensionalization.

A general trend of axial Nu_0/Nu_∞ variation in the static channel as typified in Fig. 2 is described as follows. The high Nu_0/Nu_∞ ratios in the flow entry region exhibit relatively large heat transfer variations between the rib and mid-rib locations. Streamwise distributions of Nu_0/Nu_∞ ratios gradually decay into the so called zigzag periodically developed region where a similar varying range of Nu_0/Nu_∞ between the rib and its downstream mid-rib locations remains. This zigzag periodically developed region corresponds to a pseudo developed flow region within which the rib-induced streamwise and spanwise secondary flows, as well as the spatial distributions of turbulence intensities, develop periodically with a rib pitch as the spatial period. Over the *Re* range of 5000–15,000, Nu_0/Nu_∞ ratios in the periodically developed region vary from 1.38 to 3.30. These angled ribs effectively trip the boundary layers of flow that induces the shear layers by flow separation to elevate the turbulence level. Secondary flow vortices induced by 45° surface ribs improve the fluid mixing leading to the further heat transfer enhancement. However, the local Nu_0/Nu_∞ ratios systematically fall as *Re* increases so that the relative heat transfer enhancement attributed from 45° staggered ribs is *Re* dependent. This result implies that the Nu_0 correlation is no longer the function of $Re^{0.8}$ but the exponent of *Re* is less than 0.8 in a rib-roughened channel; a well known feature of convection experimental work for ribbed duct flows [22,23]. Han groups [22,23] have presented the experimental results of turbulent heat transfers in rectangular channels of an aspect ratio 1/2 with two opposite walls roughened by 45° staggered ribs. These sets of independently tested heat transfer data are reproduced in Fig. 2 to compare with the present data for validation. Relatively large ranges of heat transfer variations between the rib and mid-rib locations have been similarly detected in the flow entry region [23] as shown in Fig. 2. With the present data

shown in Fig. 2, the best approach to the periodically developed region is taken to occur at an axial location of $3d$ that agrees closely with the compared data trends [22,23]. Since the local values of present Nu_0/Nu_∞ ratios also fall in the data ranges of [22,23] in the periodically developed region, the main agreement between the present and compared heat transfer data is very good at zero rotation. These test results with zero rotational speed confirm that the experimental facilities are performing satisfactorily and that a set of reference data-base to assess the rotational effects has been established. This set of zero rotation heat transfer data is summarized into the Nu_0 correlation with a general form of

$$Nu_0 = A(x/d) \times Re^{n(x/d)} \tag{8}$$

Coefficients A and n in Eq. (8) is x/d dependent to reflect the influence of boundary layer developments and rib-induced secondary flows along the leading and trailing surfaces. Table 3 summarizes the correlated coefficients A and n along the centerlines of leading and trailing surfaces.

Eq. (8) for Nu_0 is taken as the benchmark correlation to generate the heat transfer references at zero rotational speed for assessing the influences of rotation on heat transfer.

3.2. Rotational heat transfer results

Rotation induced Coriolis secondary flows interact with rib-induced secondary flows by means of vortex cancellation or enhancement in a channel fitted with angled ribs. These vortical interactions vary with the direction of angled ribs, the aspect ratio of rectangular channel and the angle of channel orientation [24,25]. Rib-induced vortices always flow in the rib-wise direction along the ribbed surfaces either from the bottom to top sidewalls or in a reverse manner; depending on the skewed direction of the angled ribs. But the directions of Coriolis secondary flows *relative to* the rib-induced vortices vary with the angle of channel orientation. Manners of local vortical cancellations or enhancements between the secondary flows induced by Coriolis forces and angled ribs therefore vary with the angle of channel orientation. For this reason the generalized rotational influences on heat transfer are discussed using the data collected from the rotating channel with 0° orientating angle. Impacts of channel orientation on rotational heat transfer are discussed later after all data trends describing the generalized rotational effects are discussed.

Interactive effects of vortical cells induced by Coriolis forces and angled ribs distort the axisymmetric wall temperature profiles along the test channel with the leading surface constantly operating at the higher temperatures than those on the trailing surface. The spanwise, streamwise and rib-wise variations of fluid temperatures trigger an intricate buoyancy interaction in a rotating channel. As typified in Fig. 3 with $Re = 10{,}000$ and $Ro = 0.7$, the combined effects of angled ribs, Coriolis forces and rotating buoyancy generate two separate sets of zigzag Nu profiles along the leading and trailing edges with sensible data spreads driven by varying the buoyancy level. These compound effects make the trailing-edge consistently operating at the higher heat transfer rates than its leading edge counterparts, having a downward data spread driven by the increase of $\Delta\rho/\rho$ at each axial station. Earlier rotational experiments undertaken by Morris and Aythan [26] with the lower Re range of 5000–15,000 found that buoyancy interactions impair local heat transfer for relatively low flow rates. A simple analogy of mixed convection was drawn between downward flow in a vertical pipe influenced by gravitational buoyancy [14,26]. Although this analogy could offer a possible interpretation of rotating buoyancy effect on heat transfer at that time, Iskakov and Trushin [27] has been the first demonstration that rotating buoyancy could have either an enhancing or impairing effect on heat transfer; depending on the operating flow parameters for a rotating channel. In this respect, Murata and Mochizuki [28] recently proposed another analogy based on the local interaction of Coriolis force and buoyancy by assuming the adding and opposing buoyant flows on the trailing and leading surfaces respectively. Leading-wall heat transfers are initially impaired and followed by a subsequent recovery as buoyancy enhances; while the

Table 3
Correlative coefficients A and n for Nu_0

Axial location	x/d	Leading-edge		x/d	Trailing-edge	
		$A(x/d)$	$n(x/d)$		$A(x/d)$	$n(x/d)$
Rib 1				0.5	2.21	0.43
Rib 2	1	1.82	0.43	1.5	1.21	0.47
Rib 3	2	0.82	0.5	2.5	1.12	0.48
Rib 4	3	0.81	0.51	3.5	0.86	0.50
Rib 5	4	0.76	0.52	4.5	0.74	0.52
Mid-rib 1–2	0.5	1.99	0.4	1	0.95	0.48
Mid-rib 2–3	1.5	1.02	0.47	2	0.94	0.48
Mid-rib 3–4	2.5	0.65	0.51	3	0.92	0.48
Mid-rib 4–5	3.5	0.60	0.53	4	0.89	0.49
Mid-rib 5–6	4.5	0.55	0.54			

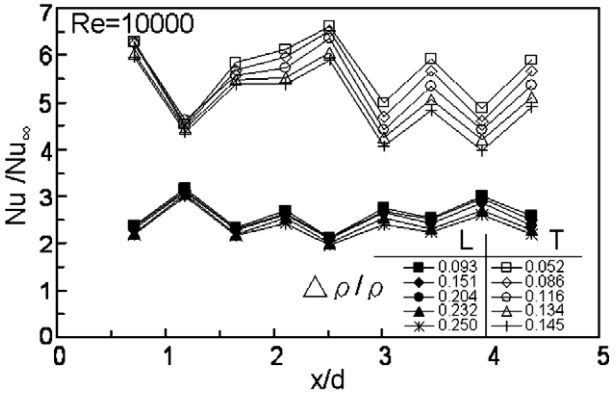

Fig. 3. Local Nusselt number distributions along leading and trailing edges for various $\Delta\rho/\rho$ at $Re = 10{,}000$ and $Ro = 0.7$.

trailing-wall heat transfers are constantly improved by rotating buoyancy effects [28]. However, with the higher *Re* range of 10,000–35,000 and speed of 0–2000 rev/min, buoyancy interactions consistently improved local heat transfers along two opposite leading and trailing edges for both smooth-walled circular tube and rib-roughened square duct [29]. In their study [29], it is worth noting that the presence of surface ribs has considerably suppressed the impacts of rotating buoyancy on heat transfer from the smooth-walled conditions. The suppression of heat transfer rates along the trailing-centerline of rotating ribbed floor for the present test channel is different from those reported in [5,7,15,25] but agrees with the studies of [26,8]. It is worth noting that the thermal boundary condition simulated by the present test channel has all the faces of each rib to be uniformly heated. This thermal boundary condition is different from the heating conditions examined by most of the previous studies [1,3–29] which could lead to the different *Bu* effects along the trailing-centerline. Nevertheless, the effects of rotating buoyancy on heat transfer are *Re* and/or *Ro* dependent but the *Bu* impact at high *Re*, *Ro* and *Bu* encountered in a real engine situation seems to remain unclear due to the various *Bu* impacts reported to date.

By way of comparison with Nu_∞, rotational heat transfer results are expressed as the Nusselt number ratios (Nu/Nu_∞). Fig. 4a and b depict the Nu/Nu_∞ ratios along leading and trailing edges at rotation numbers of 0, 0.1, 0.3, 0.5, 0.7, 1, 1.5 and 2 at Reynolds number of 5000. Spatially averaged density ratios ($\Delta\rho/\rho$) along the leading and trailing edges for the data collected in Fig. 4 are selected as 0.206 and 0.074 respectively. As well as a reconfirmation, trailing-edge heat transfers systematically increase as *Ro* increases from 0 to 2. Heat transfer ratios along the leading edge are initially decreased from the zero speed references as *Ro* increases from 0 to 0.1. This immediate heat transfer reduction that reduces the leading edge heat transfers from Nu_0 is followed by a subsequent systematic recovery as *Ro* continuously increases. Leading edge heat transfers become higher than the zero speed datum as $Ro \geqslant 1$. In a rotating rectangular channel fitted with 45° ribs, this is the first time to report the critical rotation number above which the heat transfer levels along the stable wall show enhancements from the zero speed datum. Although a streamwise decay of the varying range in zigzag Nu/Nu_∞ profiles along both leading and trailing edges as shown in Fig. 4 still follows the data trend of Fig. 2 for static channel, the rotational complexities considerably amplify the downstream zigzag variations on the trailing surface. Previous rotating flow measurements using a one-side rib-roughened channel have shown the elongated and shortened reattachment lengths from the zero speed condition on the stable and unstable rib-roughened walls respectively [30]. Rotation induced flow instabilities are likely to promote the flow mechanism that contributes to the generation of spatial heat transfer variations between a rib pitch on the trailing-wall, such as the rib-triggered separated flows and the modified turbulence structures. The *Ro* controlling local heat transfer variations along leading and trailing edges as demonstrated in Fig. 4 are similarly detected for all *Re* tested with five different heat flux settings.

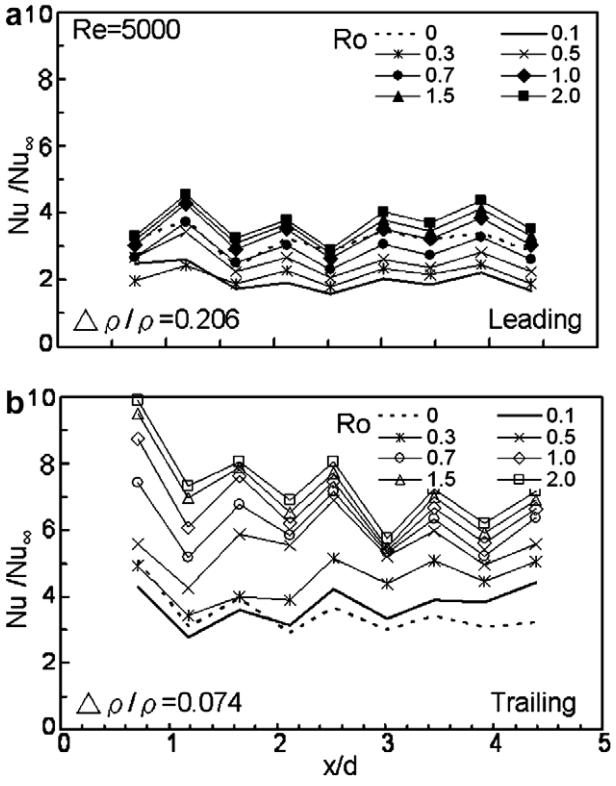

Fig. 4. Axial heat transfer distributions along (a) leading-edge ($\Delta\rho/\rho = 0.206$) and (b) trailing-edge ($\Delta\rho/\rho = 0.074$) at $Re = 5000$ with $Ro = 0$, 0.1, 0.3, 0.5, 0.7, 1, 1.5 and 2.

The rotational heat transfer data shown in Fig. 4 is affected by the combined *Re*, *Ro* and *Bu* impacts. Disengagements of interactive *Re*–*Ro*–*Bu* impacts unravel the individual influences of *Re*, *Ro* and *Bu* on rotational heat transfer. Initially, it is assumed that the *Re* effect can be uncoupled from *Ro*–*Bu* impacts by the functional relationship developed in the static channel using Eq. (8). This is testified by comparing five sets of normalized $Nu/Re^{n(x/d)}$ data obtained with different Reynolds numbers but at a fixed rotation number. The isolation of *Re* effect from *Ro*–*Bu* impacts requires the demonstration of independency of Nu/Re^n against *Re* at each fixed rotation number. Fig. 5 testifies this hypothesis by comparing the axial distributions of normalized Nusselt numbers (Nu/Re^n) along leading and trialing edges at Reynolds numbers of 5000, 7500, 10,000, 12,500 and 15,000 for a fixed rotation number of 0.1, 0.3, 0.5, 0.7 or 1. Density ratios ($\Delta\rho/\rho$) are controlled at the similar levels for each comparative case with a fixed rotation number. As shown in Fig. 5, the ranges of data spreads at each axial station gradually converge as the airflow travels downstream. Tight data bands are found in the periodically developed region. Accompanying with the streamwise convergence of data bands driven by *Re* varia-

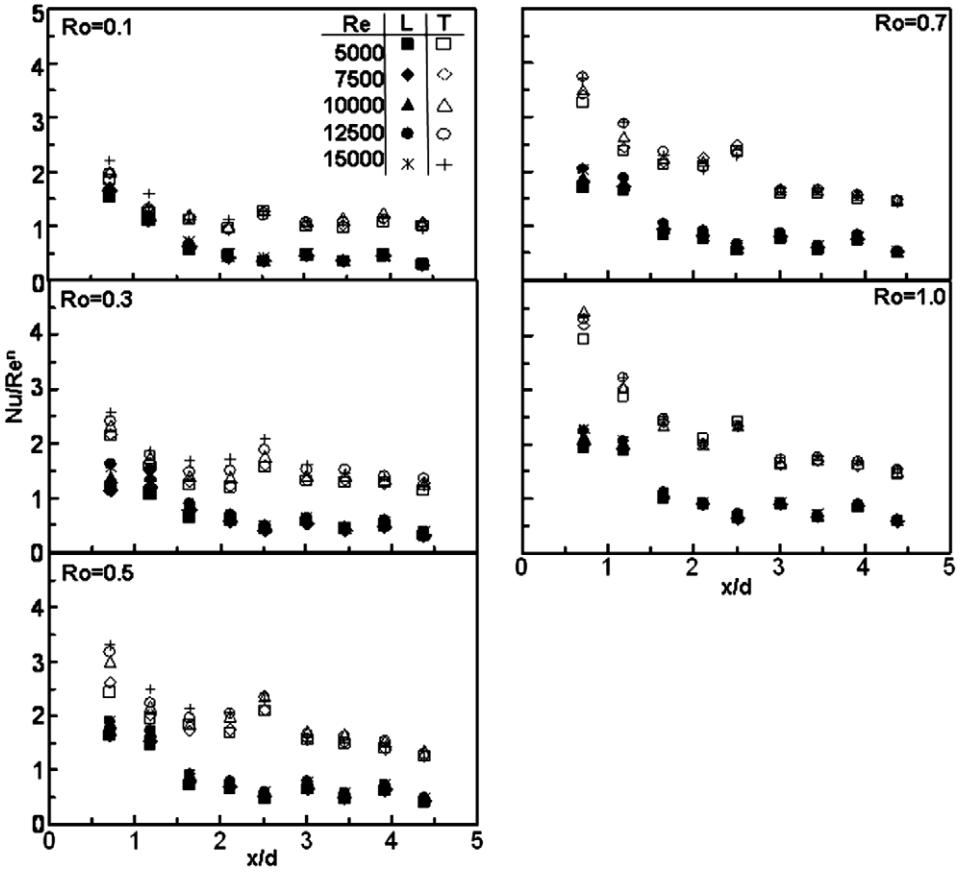

Fig. 5. Axial distributions of scaled Nusselt number with various Re along leading-edge ($\Delta\rho/\rho = 0.206$) and trailing-edge ($\Delta\rho/\rho = 0.074$) at $Ro = 0.1$, 0.3, 0.5, 0.7 and 1.

tion, the leading-to-trailing differences in Nu/Re^n increase in the downstream direction over the developing flow regime as $Ro \leqslant 0.5$. This features the growth of Coriolis and rib-induced secondary flows that establishes the well-developed peripheral heat transfer variations around the channel. The scattering Nu/Re^n data in the entry region illustrates the existence of interactive Re–Ro–Bu impacts. The downstream developments of Coriolis and rib-induced secondary flows, as well as the developing thermal boundary layers, feature an interactive flow mechanism that produces complex Re–Ro–Bu effects on entry-region heat transfer. Following the downstream developments of thermal boundary layers, Coriolis secondary flows and rib-induced vortical cells, the inter-correlation of Re in the Re–Ro–Bu functional complexities is gradually weakened in the streamwise direction. The converged data bands along leading and trailing-edges in the periodically developed region, as demonstrated in Fig. 5, enable the individual Re impact on heat transfer to be isolated from Ro–Bu effects using Nu/Re^n structure. The exponent (n) of Re is a spatial function of rib and mid-rib locations.

A subsequent data analyzing procedure is developed to unravel the isolated Ro–Bu effects on heat transfer in the periodically developed flow region. The variation of Nu/Re^n data with Bu at a fixed Ro shows the rotating buoyancy effect at each Ro and Fig. 6 typifies the buoyancy trends found. Each Nu/Re^n trend in this figure is constituted by the data acquired from all Re tested with a fixed Ro at the axial locations representing the best approach to periodically developed flow region. At each tested rotation number, there is a systematic tendency for the Nu/Re^n data to decrease with increasing Bu. The slope of each Ro controlled data series decreases with increasing Ro. A physical implication is the weakened Bu impact on heat transfer as Ro increases. The interactive Ro–Bu influence on heat transfer is demonstrated. Separations of Ro effects from the Ro–Bu interactions using the direct heat transfer measurements are not practical as a finite value of $T_w - T_b$ is necessary to define Nu. Heat transfer levels at the limiting case of $\beta(T_w - T_b) = 0$ but $Ro \neq 0$ that feature the simulated conditions in the rotating channel with zero-buoyancy are generated using the regression analysis. This regression-type curve fitting for each series of data trend at a fixed Ro in Fig. 6 can extrapolate the Nu/Re^n data to the limiting condition of zero Bu that gives the asymptotic heat transfer value at the corresponding Ro but with zero $\beta(T_w - T_b)$. A linear-like decrease of Nu/Re^n with increasing Bu is evident for each Ro controlling data trend. As a result of the data trends illustrated by Fig. 6 an attempt is made to define the heat transfer correlation at

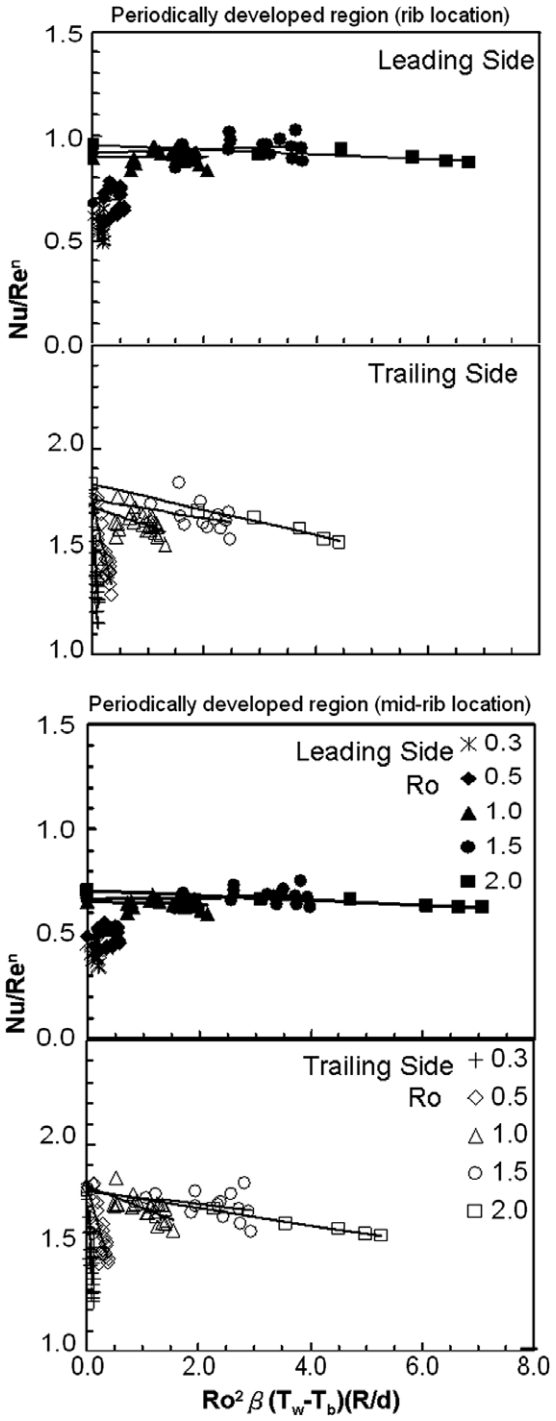

Fig. 6. Variations of scaled Nusselt number with Bu ($Ro^2\beta[T_w–T_b][R/d]$) at $Ro = 0.3$, 0.5, 1, 1.5 and 2.

the rib and mid-rib locations for flows in the periodically developed region using the equation of

$$\frac{Nu_{L,T}}{Re^n} = \phi_1\{Ro\} + \phi_2\{Ro\} \times Ro^2\beta(T_w - T_b)(R/d) \qquad (9)$$

Data trends in Fig. 6 demonstrate that ϕ_1 and ϕ_2 in Eq. (9) are functions of Ro and varied with rib and mid-rib locations. Functional values of ϕ_1 account for the rotational zero-buoyancy heat transfer data that signify the individual Ro impact on heat transfer without buoyancy interaction. The various slopes for the correlating lines in Fig. 6, as indexed by ϕ_2 functions, indicate the different degree of buoyancy impact on heat transfer that is Ro dependent. Figs. 7 and 8 depict the variations of ϕ_1 and ϕ_2 values against Ro respectively.

Variations of zero-buoyancy heat transfer data against Ro shown in Fig. 7 are treated as the isolated Ro impact on heat transfer in the periodically developed region. Trailing-edge ϕ_1 values continuously increase from the zero-rotation reference as Ro increases. The functional relationship between ϕ_1 and Ro can be assumed in a form of exponential function. The leading-edge heat transfer data is initially reduced from the zero-rotation condition as Ro increases from 0 to 0.1. A further increase of Ro from 0.3 incurs a subsequent heat transfer recovery that leads the leading-edge heat transfer to approaching the zero-speed reference. The varying manners of ϕ_1 value against Ro on the leading-edge with $Ro \geqslant 0.3$ also can be assumed as the exponential function. Rotation numbers above which the Nu/Re^n values on leading-edge become higher than the zero-rotation references are 0.68 and 1.21 at the periodically developed rib and mid-rib locations respectively. A net result of data trends on leading and trailing edges in the Ro range of $0.1 \leqslant Ro \leqslant 0.7$ is the increase of heat transfer difference between leading and trailing edges as Ro increases. This result is consistent with the growing strength of Coriolis secondary flows and the different flow instability phenomena on leading and trailing-walls. In the data range of $Ro \geqslant 1$, variations of zero-buoyancy heat transfer data on leading and trailing-walls tend to approach a similar increasing rate as Ro increases. Such heat transfer behavior leads to moderations of trailing-to-leading heat transfer differences in high Ro range ($Ro \geqslant 1$). Heat transfer results obtained with $\Delta\rho/\rho = 0.28$ are also included in Fig. 7 to depict the additional buoyancy impact on heat transfer. The two sets of heat transfer data with $\Delta\rho/\rho = 0.28$ follow the varying trends of zero-buoyancy heat transfer references. With buoyancy effects involved, heat transfer levels are constantly lower than the two sets of Ro controlled zero-buoyancy references on leading and trailing-walls. As a result, the rotation numbers above which the leading-edge heat transfers become higher than the zero-rotation heat transfer levels are increased at the periodically developed rib and mid-rib locations. This finding demonstrates that the presence of rotating buoyancy forces clearly affects the flow instability phenomena as well as the Coriolis secondary flows in the rotating rib-roughened channel. Using the manner of data presentation shown in Fig. 7 but replacing the Nu/Re^n data by Nu/Nu_0 ratio examines the relative heat transfer modifications from the zero rotational speed reference. A review of the entire set of rotational heat transfer data in terms of Nu/Nu_0 reveals that the local Nusselt number ratios are in the ranges of 0.49–1.42 and 1.08–2.73 on the leading and trailing edges respectively to reflect the interactive *Ro-Bu* effects on heat transfer.

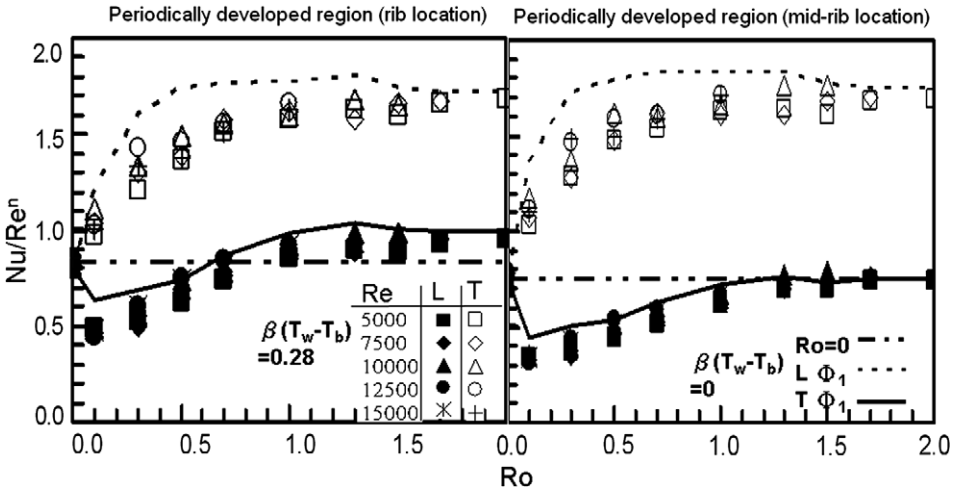

Fig. 7. Variations of scaled Nusselt number with Ro for various Re at $\beta(T_w - T_b) = 0$ and 0.28.

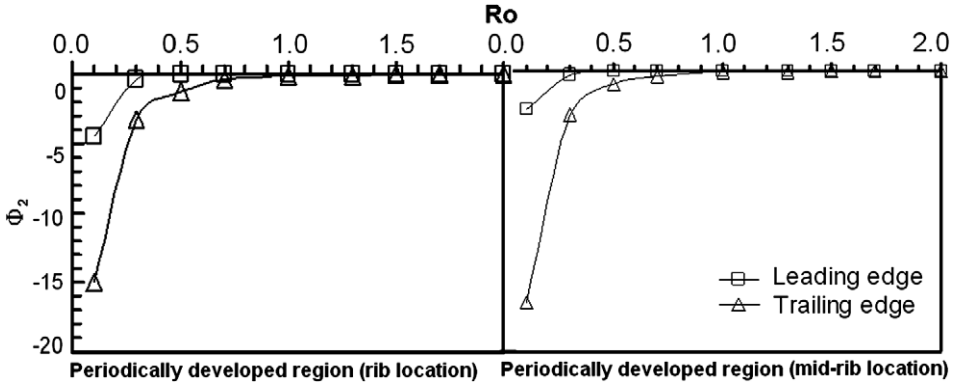

Fig. 8. Variations of Φ_2 value with rotation number.

Rotating buoyancy effects are previously examined at each tested rotation number and Fig. 6 typifies these buoyancy trends. Each data trend at a tested rotational number shows a tendency that the normalized Nusselt number (Nu/Re^n) decreases with increasing buoyancy number. The magnitude of slope, ϕ_2, for each Ro line in Fig. 6 decreases with increasing rotation number and Fig. 8 depicts the variation manner of ϕ_2 for the entire range of test undertaken. The decay of the rotating buoyancy impact as Ro increases is clearly seen in Fig. 8. Variations of ϕ_2 magnitude follow a general trend of exponential decay in Fig. 8. With Ro greater than about 0.7, ϕ_2 values that index the influence of rotating buoyancy on heat transfer are almost diminished. This result is expected that the Ro related flow physics dominate heat transfer at the higher rotation numbers. However, ϕ_2 values in Fig. 8 always remain negative in the range of $0.1 \leqslant Ro \leqslant 2$ that suggests the impairing rotating buoyancy effect on heat transfer. As ϕ_2 values vary with Ro, the coupling effects between Coriolis force and rotating buoyancy is re-confirmed.

Combinations of the regression results obtained from Figs. 6–8 derive a set of heat transfer correlations at rib and mid-rib locations on leading and trailing edges in the periodically developed region as

$$Nu_L = Re^{0.513} \times [1.19 - 0.543 \times \mathrm{Exp}(-0.411 \times Ro) + \{0.12 - 16 \times \mathrm{Exp}(-12.7 \times Ro)\} \times Bu]$$
at rib location on leading wall (10)

$$Nu_L = Re^{0.536} \times [0.697 - 0.363 \times \mathrm{Exp}(-1.56 \times Ro) + \{0.003 - 8.36 \times \mathrm{Exp}(-11.0 \times Ro)\} \times Bu]$$
at mid-rib location on leading wall (11)

$$Nu_T = Re^{0.51} \times [1.75 - 0.975 \times \mathrm{Exp}(-6.25 \times Ro) + \{-0.037 - 14.8 \times \mathrm{Exp}(-5.13 \times Ro)\} \times Bu]$$
at rib location on trailing-wall (12)

$$Nu_T = Re^{0.49} \times [1.78 - 1.03 \times \mathrm{Exp}(-9.10 \times Ro) + \{-0.108 - 37.3 \times \mathrm{Exp}(-8.32 \times Ro)\} \times Bu]$$
at mid-rib location on trailing-wall (13)

This set of heat transfer correlations has been derived following an experimental approach to resolve the influences of Re, Ro and Bu on Nusselt number. Heat transfer coefficients on the leading and trailing edges of the rotating channel can be obtained when the controlling parameter such as Re, Ro or Bu varies individually or simultaneously. The individual and interactive Re, Ro and Bu effects on heat transfer in the rectangular channel fitted with

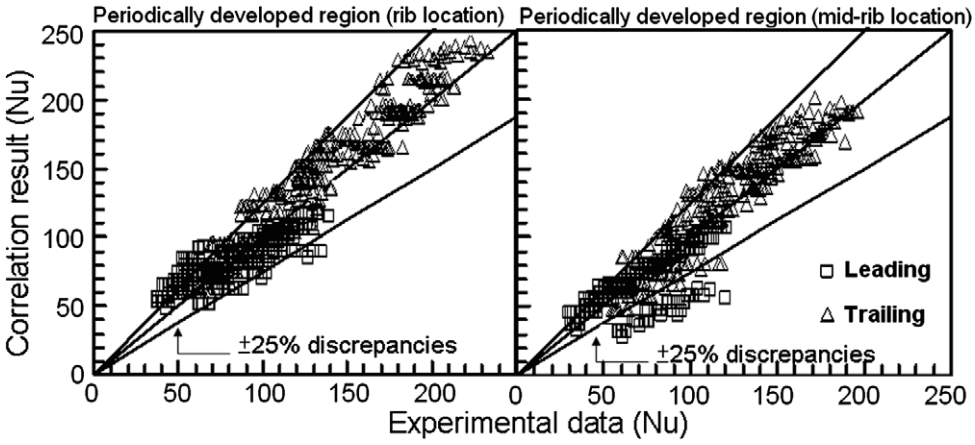

Fig. 9. Comparison of experimental measurements with correlation results.

staggered 45° ribs can be evaluated using this set of heat transfer equations. A comparison of all the experimental measurements with the correlative predictions is performed to examine the overall success of heat transfer correlations derived. As indicated in Fig. 9, 90% of the experimental data is found to agree within ±25% of the correlation proposed for the entire range of test conditions. Consider the complexities induced by the surface ribs, Coriolis force and rotating buoyancy over such wide range of rotation numbers, this set of heat transfer correlations can offer the more realistic heat transfer reference for designs of internal cooling channels in a gas turbine rotor blade.

3.3. Impact of channel orientation on rotational heat transfer

Impacts of channel orientation on heat transfer in a rotating duct fitted with angled ribs are attributed to the different modes of vortical interactions between the rib-induced and Coriolis secondary flow vortices as a result of changing the orientation angle. Variations of channel orientation for a non-circular rotating channel modify the peripheral shape that confines Coriolis secondary flows. This geometrical variation directly affects the development of Coriolis secondary flows which consequently influences the *Ro* and *Ro–Bu* controlled mechanisms. The two sets of secondary flow vortices induced by angled ribs and Coriolis forces are combined either to constructively enhance or destructively reduce the local strength of secondary flows [31]. This can be seen from the conceptual secondary flow diagrams in Fig. 1 where the secondary flow vortices induced by rotation and angled-rib for two channel orientations of 0° and 45° are compared. For the present rectangular channel depicted in Fig. 1, combinations of secondary flow vortices induced by rotation and angled-rib are in the destructive manner for the present test channel with the orientation angle of 45°. Another worth noting remark depicted in the conceptual view of secondary flow vortices shown in Fig. 1 is the deviation of leading (trailing) edge from the centerline edge on the ribbed wall as a result of increasing channel orientation from 0° to 45°. It is expected that the deviation of centerline measurements from the leading and trailing edges of a rotating duct can reduce the measured heat transfer differences between two opposite centerlines on the ribbed walls. Net results of channel-orientation impacts are illustrated by comparing the axial *Nu* distributions along two centerlines of leading and trailing walls in the channels with orientation angles of 0° and 45° as shown in Fig. 10. Heat transfer levels along the centerline of leading-wall with 45° orientation are higher than the 0° counterparts as $Ro < 0.5$. Along the centerline of trailing-wall, local Nusselt numbers in the 0° channel are consistently higher than those in the 45° channel over the entire *Ro* range tested. These comparative results caused by changing the orientation from 0° to 45° in the data range of $Ro < 0.5$ as shown in Fig. 10 agree with the previous work reported by Han group [31]. These authors [31] proposed the thinner boundary layers over the leading-wall due to the increase of channel orientation from 0° to 45° as the flow physics that enhances local heat transfers along the centerline of leading-wall in a square duct fitted with 60° angled ribs. The boundary layers over the trailing-wall are already thin and not significantly affected by the change of channel orientation; while the destructive reduction of secondary flow vortices reduces the trailing-wall Nusselt numbers in the 45° channel from the 0° references [31]. In the data range of $Ro \geqslant 1$, leading-wall heat transfers in the 45° channel become lower than those counterparts in the 0° channel. Recalling the data trends revealed in Fig. 7, the scaled Nusselt numbers along the leading centerline of the rotating channel of $\lambda = 0°$ are reverted from less than to higher than the zero-rotation-speed references in the *Ro* range of 0.5–1. Justified by the data trends compared in Fig. 10, the leading-wall heat transfers in the 45° channel turn to be less than those in the 0° channel in the *Ro* range of 0.5–1. This result implies that the rotation numbers above which the leading-wall heat transfer rates become higher than the zero-speed references are increased in the channel of $\lambda = 45°$. Evidences in this respect will be shown in Fig. 11 where the zero-buoyancy heat transfer results collected

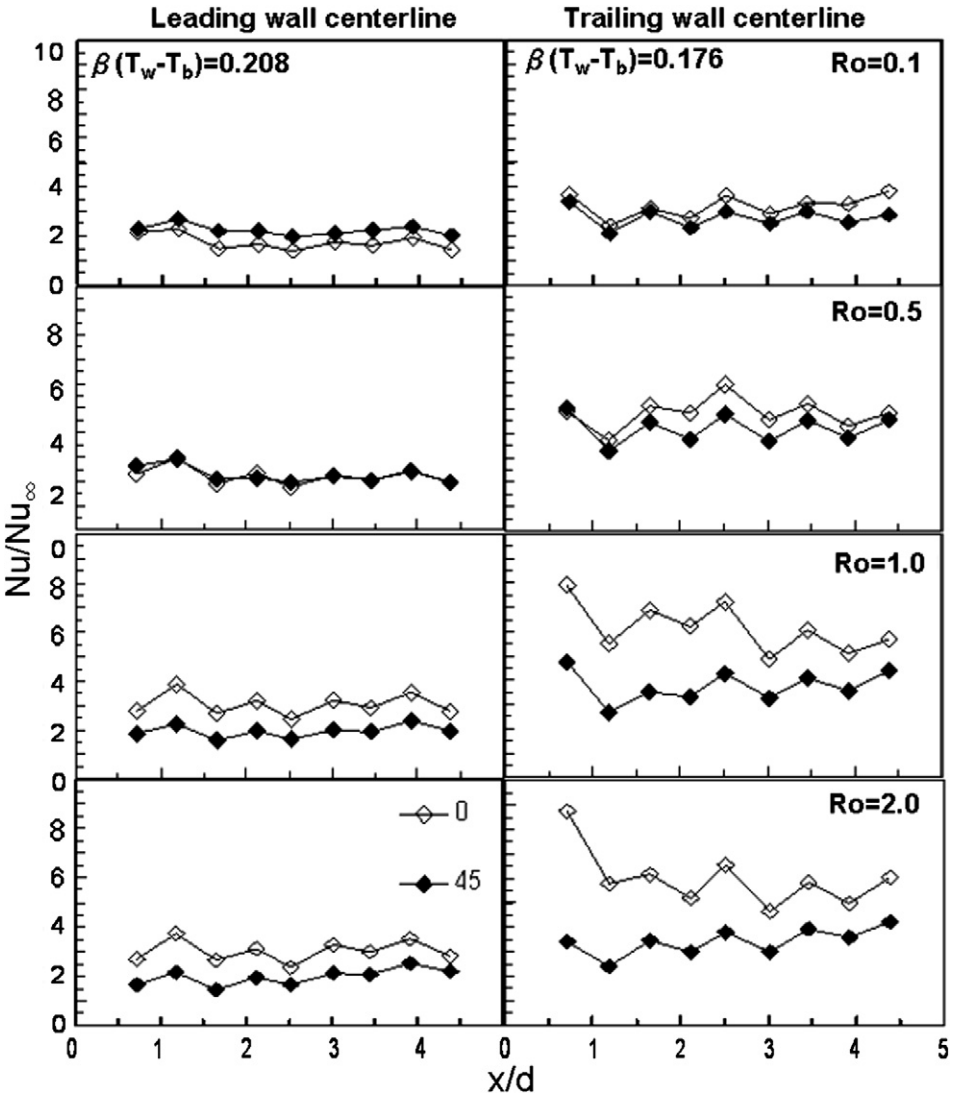

Fig. 10. Comparison of axial heat transfer variations in rotating ducts with $\lambda = 0°$ and 45° at $Ro = 0.1$, 0.5, 1 and 2.

from the channels with $\lambda = 0°$ and 45° are compared. Therefore, with the destructive manner of angled-rib arrangement in the AR = 2 rotating channel, the switch-over Ro is found as 0.5 above which the impacts of channel orientation on leading-wall heat transfer are reversed. The 0° channel consistently offers the higher trailing-wall heat transfers relative to those in the 45° channel. Along with the enhancing Coriolis secondary flows as Ro increases from 0.5 to 2, destructive reductions of local strengths of rib-induced secondary flows in the 45° channel are accordingly enhanced so that the systematic increase of heat transfers difference between 0° and 45° channels is followed as Ro increases from 0.5 to 2. Within the Ro range tested, the rotating-to-static heat transfer ratios on leading and trailing-centerlines with 45° of channel orientation are in the ranges of 0.50–1.49 and 1.06–2.21 respectively.

Variations of Coriolis force effects on heat transfer due to the change of orientation angle from 0° to 45° are best illustrated by plotting the zero-buoyancy Nu/Re^n data against Ro for both 0° and 45° channels as compared in Fig. 11. In agreement with the results unraveled in Fig. 10, leading-wall heat transfers in the 45° channel are increased from the 0° channel levels as $Ro < 0.5$. Further increases of Ro from 0.5, the leading-wall heat transfer in the 45° channel become less than those in the 0° channel. On the trailing-wall, the 0° channel consistently possesses of a higher heat transfer rate than its counterpart in the 45° channel. In the channel of $\lambda = 45°$, there is no critical Ro identified. But the critical rotation numbers above which the leading-wall heat transfers are improved from the zero-rotation references seem to be increased in the channel with orientation angle of 45° as the leading-edge heat transfer coefficients for the channel of $\lambda = 45°$ are constantly operated at the lower levels than the 0° channel as $Ro > 0.5$. Plotting the heat transfer data collected from both 0° and 45° channels in the manner constructing Fig. 8 highlights the impacts of channel orientation on the rotating buoyancy effects. Fig. 12 compares the variations

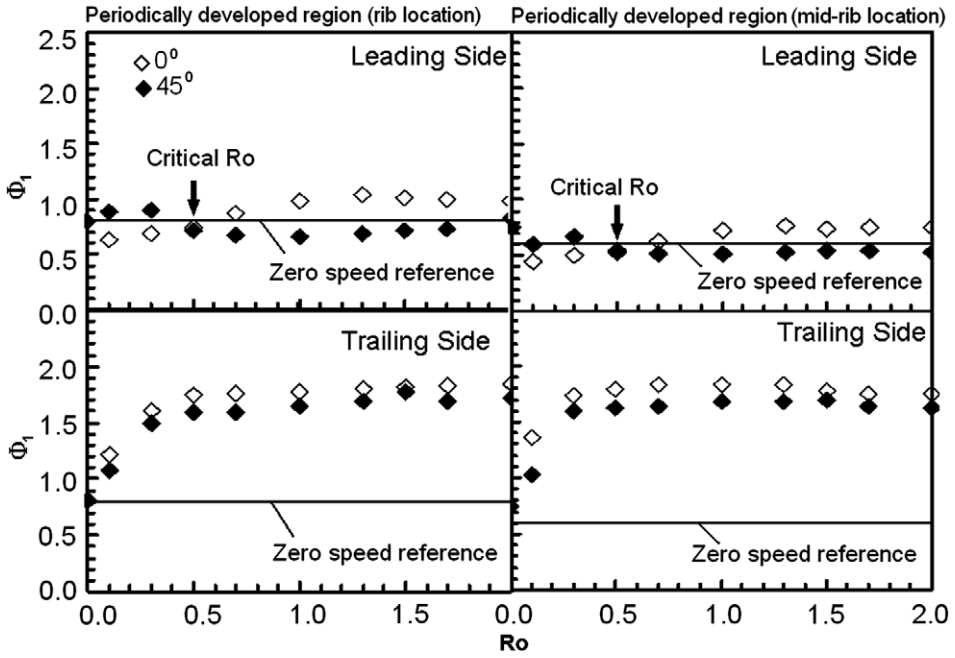

Fig. 11. Comparison of calculated zero-buoyancy heat transfers (Φ_1) in rotating ducts with $\lambda = 0°$ and 45° against *Ro*.

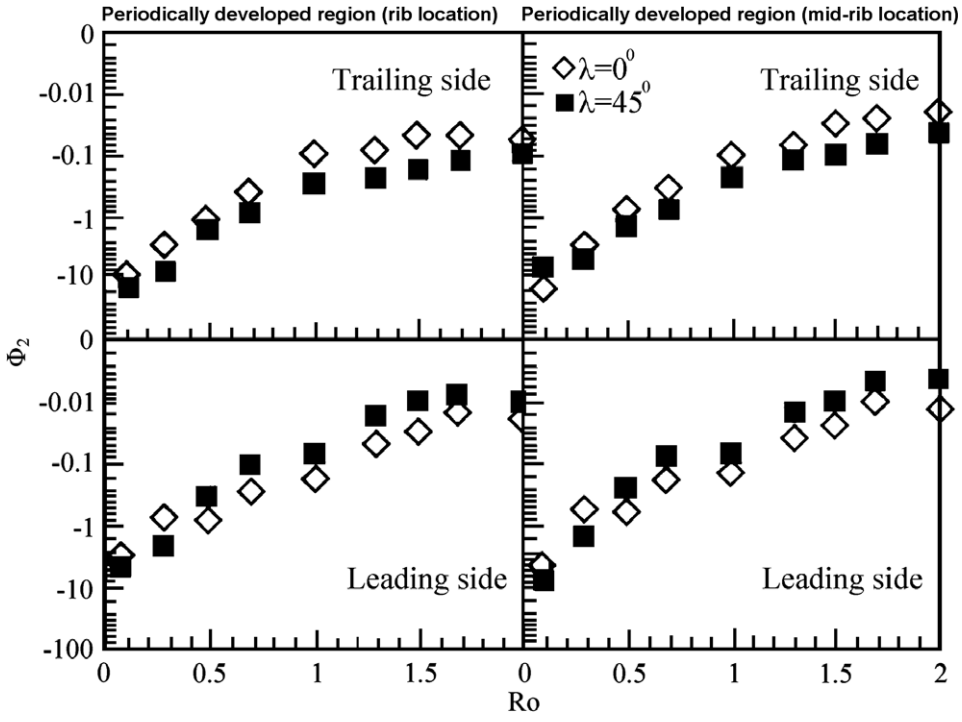

Fig. 12. Comparison of Φ_2 values in rotating ducts with $\lambda = 0°$ and 45° against *Ro*.

of ϕ_2 value against *Ro* along the leading and trailing-centerlines in both 0° and 45° channels. As indicated by all the negative ϕ_2 values shown in Fig. 12, the impairing rotating buoyancy impacts on heat transfer in both 0° and 45° channels are confirmed for the present test configuration. The larger magnitudes of ϕ_2 value in the 0° channel over the range of $Ro \geqslant 0.5$ on the leading-wall reflect the relatively stronger rotating buoyancy effects on heat transfer. On the trailing-wall, the stronger buoyancy impacts develop in the channel with 45° orientation angle. Although the data trends in both 0° and 45° channels as shown in Fig. 12 are similar, functional dependencies of ϕ_2 with *Ro* are different between the 0° and 45° channels. Interactive *Ro–Bu* impacts on heat transfer in the present

rib-roughened rotating rectangular channel are quantitatively altered by increasing the channel orientation from 0° to 45°.

4. Conclusions

This work has examined an extensive body of rotational heat transfer data in a rectangular duct fitted with 45° staggered ribs. Heat transfer results with the large range of rotation number aid greatly in the heat transfer correlation and validation of physical models and CFD codes for the complex heat transfer phenomena in a rotating channel. The salient points resulting from the present investigation are summarized as follows.

1. Axial distributions of Nu_0 profile exhibit a zigzag pattern with regions of relatively high heat transfers at the rib locations. As well as a reconfirmation, the 45° staggered ribs generate the overall heat transfer augmentation in the range of 1.6–4.3 times of Dittus–Boelter level in the *Re* range of 5000–15,000 in the channel with zero rotational speed.
2. The entry-region interactive *Re–Ro–Bu* impacts on heat transfer are gradually weakened in the downstream direction, along with the streamwise developments of boundary layers, Coriolis secondary flows and rib-induced vortical cells. The inter-correlative *Re* effect in the *Re–Ro–Bu* functional complexities for evaluating *Nu* tends to be diminished in the periodically developed region that enables the individual *Re* impact to be isolated from *Ro–Bu* interactions using Nu/Re^n structure.
3. Coriolis forces create peripheral variations in local heat transfer with a tendency to improve the trailing-edge heat transfer in relation to the leading-edge. As *Ro* increases, the trailing-edge heat transfer consistently increases from the stationary reference, but the leading-edge heat transfer is initially reduced from the stationary condition in the range of $0 \leqslant Ro \leqslant 0.1$. The further increase of *Ro* from 0.3 incurs a subsequent heat transfer recovery that leads the leading-edge heat transfer to approaching the zero-speed reference. Affected by Coriolis-forces effects alone without buoyancy interaction, the rotation numbers above which the leading-edge heat transfer is enhanced from the zero-speed reference are 0.68 and 1.21 at the periodically developed rib and mid-rib locations respectively.
4. The rotating buoyancy effect impairs the local heat transfer along leading and trailing edges. The coupling *Ro–Bu* impact drives the impairing buoyancy effect on heat transfer to decrease rapidly as *Ro* increases. With $Ro \geqslant 0.7$, the impairing buoyancy effect on heat transfer is almost diminished.
5. Local Nusselt numbers along the leading centerline of 45° channel are higher than those in 0° channel as $Ro < 0.5$. With $Ro \geqslant 1$, leading-wall heat transfer levels in the 45° channel become lower than the 0° channel references. The switch-over *Ro* above which the impacts of channel orientation on leading-wall heat transfer are reversed is found as 0.5 for the present channel configuration. Along the centerline of trailing-wall, local Nusselt numbers in the 0° channel are consistently higher than those in the 45° channel over the entire *Ro* range tested. Destructive reductions of rib-induced and Coriolis secondary flow vortices in the 45° channel considerably moderate the developing rate of heat transfer augmentation on the trailing-wall as *Ro* increases. Combined effects caused by varying channel orientation from 0° to 45° reduce the trailing-to-leading heat transfer differences in the 45° channel. Impairing rotating buoyancy effects on heat transfer remain in both 0° and 45° channels. Interactive *Ro–Bu* impacts on heat transfer are quantitatively altered by changing the channel orientation.
6. Heat transfer correlations are developed to calculate the Nusselt numbers at periodically developed rib and mid-rib locations with channel orientations of 0° and 45° that permit the individual and interactive effects of *Re*, *Ro* and *Bu* on rotational heat transfer to be evaluated.

Acknowledgement

The authors wish to express their appreciation to the National Science Council for their financial support under the grand number NSC 93-2611-E-022-004.

References

[1] D.K. Tafti, S.P. Vanka, A numerical study of the effects of spanwise rotation on turbulent channel flow, Phys. Fluids A 3 (4) (1991) 642–656.
[2] S.W. Chang, T.L. Yang, W.J. Wang, Heat transfer in a rotating twin-pass trapezoidal-sectioned passage roughened by skewed ribs on two opposite walls, Heat Transfer Eng. 27 (2006) 63–79.
[3] T.S. Griffith, L. AI-Hadhrami, J.-C. Han, Heat transfer in rotating rectangular cooling channels (AR = 4) with dimples, ASME J. Turbomachine. 125 (2003) 555–563.
[4] T.S. Griffith, L. AI-Hadhrami, J.-C. Han, Heat transfer in rotating rectangular cooling channels (AR = 4) with angled ribs, ASME J. Turbomachine. 124 (2003/2002) 617–625.
[5] L. AI-Hadhrami, T.S. Griffith, J.-C. Han, Heat transfer in a two-pass rotating rectangular channels (AR = 2) with five different orientations of 45-degV-shaped rib turbulators, ASME J. Heat Transfer 125 (2003) 233–242.
[6] S. Dutta, J.C. Han, Local heat transfer in rotating and ribbed two-pass square channels with three channel orientations, ASME J. Heat Transfer 118 (1996) 578–584.
[7] S.W. Chang, W.D. Morris, Heat transfer in a radially square duct fitted with in-line transverse ribs, Int. J. Thermal Sci. 42 (2003) 267–282.
[8] J.A.J. Khamaj, An Experimental Study of Heat Transfer in the Cooling Channel of Gas Turbine Rotor Blades, Ph.D thesis., University of Wales, Swansea (UK), 2002.
[9] T.-M. Liou, M.-Y. Chen, M.-H. Tsai, Fluid flow and heat transfer in a rotating two-pass square duct with in-line 90-Deg ribs, ASME J. Turbomachine. 124 (2002) 260–268.
[10] T.-M. Liou, M.-Y. Chen, Y.-M. Wang, Heat transfer, fluid flow, and pressure measurements inside a rotating two-pass duct with detached 90-Deg ribs, ASME Turbomachine. 125 (2003) 565–574.

[11] S.-S. Hsieh, H.-J. Chin, Turbulent flow in a rotating two pass ribbed rectangular channel, ASME J. Turbomachine. 125 (2003) 609–622.
[12] S. Fann, W.-J. Yang, N. Zhang, Local heat transfer in a rotating serpentine passage with rib-roughened surface, Int. J. Heat Mass Transfer 37 (1994) 217–228.
[13] G.J. Hwang, S.C. Tzeng, C.P. Mao, C.Y. Soong, Heat transfer in a radially rotating four-pass serpentine channel with staggered half-V rib turbulator, ASME Heat Transfer 123 (2001) 39–50.
[14] J.H. Wagner, B.V. Johnson, B.A. Graziani, F.C. Yeh, Heat transfer in rotating serpentine passages with trips normal to the flow, ASME J. Turbomachine. 114 (1992) 847–857.
[15] B.V. Johnson, J.H. Wagner, G.D. Steuber, F.C. Yeh, Heat transfer in rotating serpentine passages with trip skewed to the flow, ASME Turbomachine. 116 (1994) 113–123.
[16] H.A. Ei-Husayni, M.E. Taslim, D.M. Kercher, Experimental heat transfer investigation of stationary and orthogonally rotating asymmetric and symmetric heated smooth and turbulated channel, ASME Turbomachine. 116 (1994) 124–132.
[17] F.T. Willett, A.E. Bergles, Heat transfer in rotating narrow rectangular pin-fin ducts, Exp. Therm. Fluid Sci. 25 (2002) 573–582.
[18] W.D. Morris, A rotating facility to study heat transfer in the cooling passage of turbine blades, J. Power Eng. 210 (1996) 55–63.
[19] JHT Editorial Board of ASME J. Heat Transfer, 1993, Journal of Heat Transfer Policy on Reporting Uncertainties in Experimental Measurements and Results, ASME J. Heat Transfer, 115, 5–6.
[20] F.W. Dittus, L.M.K. Boelter, Publications in Engineering, University of California, Berkeley, CA, 2, 443.7, 1930.
[21] T.-M. Liou, J.-J. Hwang, S.-H. Chen, Simulation and measurement of enhanced turbulent heat transfer in a channel with periodic ribs on one principal wall, Int. J. Heat Mass Transfer 36 (1993) 507–517.
[22] J.C. Han, J.S. Park, Developing heat transfer in rectangular channels with rib turbulators, Int. J. Heat Mass Transfer 31 (1988) 183–195.
[23] G.S. Azad, M.J. Uddin, J.C. Han, K.-H. Moon, B. Glezer, Heat transfer in a two-pass rectangular rotating channel with 45-deg angled rib turbulators, J. Turbomachine. 124 (2002) 251–259.
[24] A.Q. Mohammad, H.C. Chen, J.C. Han, A numerical study of flow and heat transfer in rotating rectangular channels (AR = 4) with 45 Deg rib turbulators by Reynolds stress turbulence model, ASME J. Heat Transfer 125 (2003) 19–26.
[25] A. Murata, S. Mochizuki, Effect of cross-sectioned aspect ratio on turbulent heat transfer in an orthogonally rotating rectangular duct with angled rib turbulators, Int. J. Heat Mass Transfer 46 (2003) 3119–3133.
[26] W.D. Morris, T. Aythan, Observations on the influences of rotation on heat transfer in the coolant channels of gas turbine rotor blades, Proc. Inst. Mech. Eng. 193 (21) (1979) 303–311.
[27] K.M. Iskakov, V.A. Trushin, The effect of rotation on heat transfer in the radial cooling channels of turbine blades, Teploenergetika 32 (2) (1985) 52–55.
[28] A. Murata, S. Mochizuki, Effect of centrifugal buoyancy on turbulent heat transfer in an orthogonally rotating square duct with transverse or angled rib turbulators, Int. J. Heat Mass Transfer 46 (2001) 3119–3133.
[29] S.W. Chang, W.D. Morris, A comparative study of heat transfer between rotating circular smooth-walled and square rib-roughened ducts with cooling application for gas turbine rotor blades, JSME Int. J. Series B 41 (2) (1998) 302–315.
[30] P.H. Rothe, J.P. Johnston, Free shear layer in rotating systems, ASME J. Fluids Eng. 101 (1979) 117–120.
[31] J.A. Parsons, J.C. Han, Y. Zhang, Effect of model and wall heating condition on local heat transfer in a rotating two-pass square channel with rib turbulators, Int. J. Heat Mass Transfer 38 (1995) 1151–1159.